Structure determination in 55-atom Li–Na and Na–K nanoalloys

Andrés Aguado[a] and José M. López
Departamento de Física Teórica, Atómica y Óptica, Universidad de Valladolid, Valladolid 47071, Spain

The structure of 55-atom Li–Na and Na–K nanoalloys is determined through combined empirical potential (EP) and density functional theory (DFT) calculations. The potential energy surface generated by the EP model is extensively sampled by using the basin hopping technique, and a wide diversity of structural motifs is reoptimized at the DFT level. A *composition comparison* technique is applied at the DFT level in order to make a final refinement of the global minimum structures. For dilute concentrations of one of the alkali atoms, the structure of the pure metal cluster, namely, a perfect Mackay icosahedron, remains stable, with the minority component atoms entering the host cluster as substitutional impurities. At intermediate concentrations, the nanoalloys adopt instead a core-shell polyicosahedral (p-Ih) packing, where the element with smaller atomic size and larger cohesive energy segregates to the cluster core. The p-Ih structures show a marked prolate deformation, in agreement with the predictions of jelliumlike models. The electronic preference for a prolate cluster shape, which is frustrated in the 55-atom pure clusters due to the icosahedral geometrical shell closing, is therefore realized only in the 55-atom nanoalloys. An analysis of the electronic densities of states suggests that photoelectron spectroscopy would be a sufficiently sensitive technique to assess the structures of nanoalloys with fixed size and varying compositions. © *2010 American Institute of Physics*. [doi:10.1063/1.3479396]

I. INTRODUCTION

Bimetallic nanoparticles (or nanoalloys) have recently attracted a lot of attention due to the fact that their physical and chemical properties depend not only on cluster size but also on their composition and specific chemical ordering. They are also interesting from a fundamental point of view, as they may present structures that are very different from those of the corresponding pure metal clusters and display different properties as compared to the corresponding bulk alloys due to the finite size effects. Some elements that are immiscible in the bulk limit may mix at the nanoscale, allowing the study of the properties of new materials that are only stable as finite size systems. It is therefore no surprise that the number of experimental[1–6] and theoretical[7–32] investigations on nanoalloys has increased a lot in recent years. An extensive review article[33] includes many other references to previous works.

The most fundamental property of an atomic cluster at sufficiently low temperatures is its global minimum (GM) structure. From a theoretical point of view, locating the GM structure of nanoalloys is an extremely difficult problem. The potential energy surface (PES) of $A_x B_{N-x}$ nanoalloys presents an increased complexity as compared to the PES of pure metal clusters due to the presence of *homotops*,[8] i.e., structures with the same number of atoms N, composition x, and geometrical arrangement of atoms, which differ only in the specific allocation of A and B atomic species over the atomic sites. The isomer spectrum is therefore much denser than for pure metal clusters, and high-energy barriers may separate the different homotops associated to a single struc-

tural motif. These difficulties are further exacerbated by the need of employing a first-principles approach in order to determine realistic structures; as usual, EPs do not describe the quantum electronic shell effects, for example. In this respect, a combined EP/DFT approach, in which a wide diversity of the structural motifs generated at the EP level are reoptimized at the DFT level, has proven to be most effective.[23]

An initial attempt toward a systematic understanding of structural trends in nanoalloys has been performed by Doye and Meyer,[16] who made available the GM structures of binary Lennard-Jones (BLJ) clusters in the Cambridge Cluster Database.[34] However, the BLJ model is not representative of metallic bonding, and most works on bimetallic nanoalloys have been restricted to transition metals.[21–23,25–32] From a fundamental point of view, it is a good idea to analyze the structural trends in metallic nanoalloys formed by combining two alkali metals. Pure alkali clusters have been instrumental in our present understanding of metal cluster properties,[35,36] and their mixtures might play a similar role in nanoalloy physics.

Previous work on alkali binary clusters is rather scarce. Hristova *et al.*[24] reported the GM structures of equiatomic K–Cs and Rb–Cs nanoalloys at the EP level. They observed a preference for p-Ih packing and core-shell segregation, in agreement with results by Aguado *et al.*[12–15] for other alkali nanoalloys. A goal of the present study is to show that EP results are not quantitative for these systems as quantum electron shell effects play an important role. On the experimental side, Tchaplyguine *et al.*[6] found evidence for core-shell segregation in Na–K nanoalloys by using synchrotron-based photoelectron spectroscopy.

---

a)Electronic mail: aguado@metodos.fam.cie.uva.es.

In this paper, we report the putative GM structures of 55-atom Li–Na and Na–K nanoalloys, for which the size mismatch and bond strength difference are as small as possible for alkali elements. We have chosen 55-atom clusters because the GM structure of the pure alkali clusters is a perfect Mackay icosahedron, and it is interesting to analyze the stability of this geometrical shell closing upon doping. The jellium model[36] predicts a prolate shape deformation for 55-atom metal clusters, but this is not realized in pure alkali clusters due to the high structural stability of the icosahedron. If a different structural motif is more stable for the nanoalloys, the jelliumlike predictions might induce substantial shape changes as compared to the pure metal clusters. The theoretical approach for locating the GM structures is described in Sec. II. Section III describes the structures and also some electronic properties of the nanoalloys and tries to motivate experimental studies on these systems. Section IV offers some concluding remarks.

II. COMPUTATIONAL METHODS

A. Empirical potential models

We have chosen two different EPs to generate an approximate PES for alkali nanoalloys. In the Gupta potential,[37–40] the total energy of an A_xB_{N-x} nanoalloy is a sum of atomic contributions $E_{i,\alpha}$, where $i=1,\dots,N$ labels the atom and $\alpha=A,B$ are the atomic species. Each atomic contribution is decomposed into an attractive band-energy many-body term $E_{i,\alpha}^{\text{band}}$ and a repulsive pairwise contribution $E_{i,\alpha}^{\text{rep}}$,

$$E_{i,\alpha} = E_{i,\alpha}^{\text{band}} + E_{i,\alpha}^{\text{rep}}, \tag{1}$$

$$E_{i,\alpha}^{\text{band}} = -\left\{ \sum_{j\neq i}^{N} \sum_{\beta=A,B} n_{j\beta}\xi_{\alpha\beta}^2 \exp\left[-2q_{\alpha\beta}\left(\frac{r_{ij}}{r_{\alpha\beta}^0}-1\right)\right]\right\}^{1/2}, \tag{2}$$

$$E_{i,\alpha}^{\text{rep}} = \sum_{j\neq i}^{N} \sum_{\beta=A,B} n_{j\beta}A_{\alpha\beta}\exp\left[-p_{\alpha\beta}\left(\frac{r_{ij}}{r_{\alpha\beta}^0}-1\right)\right], \tag{3}$$

where r_{ij} is the distance between atoms i and j and $n_{j\beta}$ is 1 if atom j belongs to species β and zero otherwise. $q_{\alpha\beta}$ and $p_{\alpha\beta}$ are dimensionless parameters that determine the spatial range of the band and repulsive terms, respectively, while $\xi_{\alpha\beta}$ and $A_{\alpha\beta}$ fix the strength of those terms and have units of energy. Usually, $r_{\alpha\alpha}^0$ is the bulk nearest-neighbor distance. The Gupta potential thus naturally describes the size mismatch and bond strength effects. Through the many-body term, it also reproduces the bond order-bond length correlations leading, in particular, to a contraction of bond lengths at the surface of a metal.

For homoatomic interactions (AA and BB terms), the parameters have been determined by Li et al.[41] For 55-atom alkali clusters, this potential leads to the correct GM structure, namely, a perfect Mackay icosahedron. Therefore, we have adopted this set of parameters in our study without further optimization. In the heteroatomic AB interactions, we have chosen $r_{AB}^0 = \frac{1}{2}(r_{AA}^0 + r_{BB}^0)$. Regarding the other four pa-

rameters, we have tested several mixing rules[42] but have not found substantial differences between the GM structures predicted by them. As the main goal of the EP calculations here is to generate a diverse set of initial structures as an input for DFT reoptimization, we have adopted simple Lorentz mixing rules (arithmetic mean) for all heteroatomic parameters. Optimal heteroatomic parameters have been found to be close to the average values for alkali[43] and other metallic alloys.[39]

We have also employed the BLJ potential in order to generate more diversity. The homoatomic parameters are fixed by the experimental lattice constants and cohesive energies of the bulk metals. The heteroatomic parameters are obtained from Lorentz mixing rules.

B. Unbiased structure optimization

The PES generated by the EP models has been sampled through the basin hopping (BH) algorithm.[44,45] The essence of the BH method is a mapping of the original PES into a stepwise modified PES obtained by local optimization. In the transformed PES, there are plateaus associated with local minima and discontinuous steps separating the different local minima. In this way, energy barriers are substantially decreased so that a Monte-Carlo sampling is more efficient than on the original PES.

We have employed two different moves: (a) random displacements of all atoms and (b) swap moves in which the identity of two randomly chosen A- and B-atoms is interchanged. The first move allows to sample different structural isomers, while the second one allows to sample the different homotops for each structural isomer. We found optimal to employ 80% moves of type (a) and 20% moves of type (b) in our BH runs.

For each composition x, we performed several (between 20 and 50, depending on composition) BH runs, all starting from an initial random structure and with the thermal energies ranging from $k_BT=0.01-0.2$ eV for the (a)-type moves. An independent temperature is used for the swap moves, which is within the range of $k_BT=0-0.03$ eV. The runs are at least 3×10^6 steps long. A final BH run incorporating only swap moves is performed on the few lower energy structural motifs. With these settings, we are able to locate the same putative GM structures in different BH runs for each composition. After the runs, we store the 2000 cluster configurations of lowest energy.

C. DFT reoptimization

The first-principles calculations have been performed at the Kohn–Sham[46] DFT (Ref. 47) level (SIESTA code[48]) within the spin-polarized local density approximation (Perdew–Zunger parametrization[49,50]) and employing norm-conserving pseudopotentials.[51,52] The basis set is of "double zeta plus polarization" quality. The fast-Fourier-transform mesh cutoff[48] is 100 Ryd. Tests were performed within the spin-polarized generalized gradient approximation in its PBE implementation[53] for specific compositions. The relative stabilities of the different isomers were very similar, suggesting that LDA is sufficient for the simple metals studied here.

A crucial point of our study is to consider the potential as a generator of structural diversity and to choose a few homotops of each structural motif for DFT reoptimization.[23] We have chosen 80 different configurations for each composition: the 30 lower energy isomers from the Gupta runs, ten isomers from the BLJ runs, and 40 additional configurations chosen from the high-energy isomers (either Gupta or BLJ) according to the values of structural indicators. For example, the Hill–Wheeler parameters[54] are obtained from the principal moments of inertia $I_1 \geq I_2 \geq I_3$ as follows:

$$I_k = \frac{2}{3}r^2\left(1 + \beta \sin\left(\gamma + \frac{(4k-3)\pi}{6}\right)\right), \qquad (4)$$

$$I_1 + I_2 + I_3 = 2r^2, \qquad (5)$$

where all atoms are assigned the same mass (1 amu). r is the root-mean-square radius of the cluster, β measures the degree of quadrupole deformation, and γ determines if the shape is prolate or oblate. $\gamma = 0$ corresponds to prolate (cigar-like), $\gamma = \pi/3$ to oblate (pancake). For intermediate γ values, cluster deformation is triaxial. If $\beta = 0$, then the shape is spherical. If $\gamma = \pi/3$, the maximum value of β is 0.5 (a disk of zero thickness). If $\gamma = 0$, then the maximum value of β is 1 (a linear chain).

The Hill–Wheeler parameters are relevant here because, according to the jellium model,[36] the bunching of electronic energy levels into shells is strongly influenced by the cluster shape. For 55-atom clusters, the jellium model predicts a prolate deformation.[55] This is not observed in pure alkali clusters because of the high stability (geometrical shell closing) of a perfect icosahedron but might be relevant for 55-atom nanoalloys. We therefore choose 20 additional conformations from the EP database, taking different degrees of prolate/oblate/triaxial shape deformations. Another structural indicator is the number of core atoms N_c. Usually the EPs strongly favor structures with a given value of N_c. The 20 final conformations are chosen from the lower energy isomers which have $N_c \pm 1$ or $N_c \pm 2$ core atoms.

After DFT optimization of these structures, we start a refinement procedure based on *composition comparison*.[23] Specifically, for each composition x, we generate new structures by transmuting an A-atom into a B-atom (or vice versa) in the lowest-energy structure of the neighboring compositions $x \pm 1$. We do this in all possible ways, except when the surface segregation of one atomic species is clearly identified. The many new isomers thus generated are locally optimized at the DFT level. When this process results in a better putative GM for a certain composition, it is considered as the seed for the next iteration of the composition comparison cycle, which is continued until no better isomers are generated. At this point, more than 200 different isomers have been fully optimized at the DFT level for many values of x (on average, about 150 isomers for each composition). Although this is computationally intensive, it is still at least one order of magnitude less expensive than optimizing all the isomers 0.2–0.3 eV above the Gupta GM.

In order to analyze the stability of the obtained structures, we have calculated the cluster cohesive energies,

$$E_{\text{coh}}(A_xB_{55-x}) = -\frac{E(A_xB_{55-x}) - xE(A) - (55-x)E(B)}{55}, \qquad (6)$$

where $E(A_xB_{55-x}) = E(x)$ is the total energy of the nanoalloy and $E(A)$, $E(B)$ are the energies of the isolated atoms. We have also calculated excess energies defined by[33]

$$E_{\text{exc}}(A_xB_{55-x}) = E(A_xB_{55-x}) - x\frac{E(A_{55})}{55} - (55-x)\frac{E(B_{55})}{55}, \qquad (7)$$

where $E(A_{55})$, $E(B_{55})$ are the energies of the pure 55-atom clusters in their GM structure. Negative excess energy values indicate that formation of the corresponding nanoalloy is energetically favorable. We finally calculate the second-order difference,

$$\Delta_2(A_xB_{55-x}) = E(x+1) + E(x-1) - 2E(x). \qquad (8)$$

A large and positive Δ_2 indicates that the nanoalloy is very stable compared to the two nanoalloys with neighboring compositions.

Several electronic properties have also been calculated: atomic partial charges, electronic densities of states (DOS), and vertical ionization potentials (VIP) and electron affinities (VEA). The two latter quantities are obtained by explicitly calculating the DFT total energies of the singly charged cation and anion clusters while keeping their structures frozen at the neutral GM geometry. The electronic DOS have been obtained by homogeneously shifting all Kohn-Sham eigenvalues in such a way that the highest occupied molecular orbital (HOMO) matches the theoretical VIP value and broadening the electronic levels with Gaussian functions of width 0.05 eV. We have shown[56,57] that these settings provide a close agreement with experimental VIP values and also with photoelectron spectra in simple metallic clusters.

We evaluate the atomic charges with two methods based on a direct partitioning of the electron density distribution: the Voronoi Deformation Density (VDD) charges[58] and the Atoms-in-Molecules Bader charges,[59] as modified by Spackman and Maslen.[60] In the VDD method, the atomic boundaries are defined by the faces of the corresponding Voronoi polyhedron, so the different sizes of different atomic species are not properly described. The Bader method locates instead the zero-flux surfaces of the electron density field, which then divide the molecule into atomic regions. This method accounts in a natural way for the differences in atomic sizes, but it may lead to geometrically complex atomic basins.

III. RESULTS

A. Model potential structures

Figure 1 shows a representative selection of the putative GM structures of Li_xNa_{55-x} according to the Gupta model. Different structural motifs dominate over selected composition intervals. At some well defined compositions (*critical compositions* hereafter), a structural transition occurs. In the dilute concentration limits, the perfect icosahedral structure of the metal host remains stable upon substitutional doping.
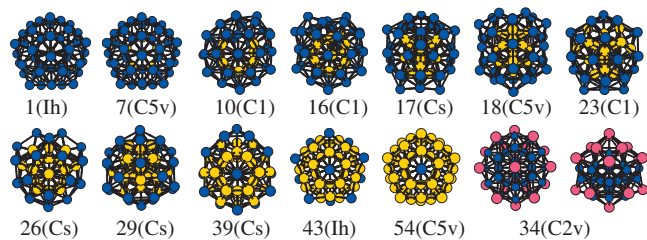
FIG. 1. Putative GM structures and point group symmetries predicted by the Gupta potential. Yellow, blue, and pink represent Li, Na, and K atoms, respectively.

For $x=1$, the Li impurity occupies the central position in the icosahedron. For $x=2-7$, the Li atoms substitute other internal sodium atoms, so there is a clear segregation of the Li component into the cluster core. The core, a 13-atom icosahedron, is itself segregated (for example, for $x=7$, the Li atoms form a pentagonal bipyramid). In the Li-rich limit, the icosahedron remains stable for compositions $x=43-54$: each additional Na atom occupies now a vertex site at the surface. However, there is no segregation of Li and Na components within the surface shell, as there are no Na–Na bonds. For $x=43$, all the vertex sites of the Mackay icosahedron are occupied by Na atoms, and a high-symmetry structure results.

A new structural motif becomes most stable for $x=8-12$. Its core is based on the Z14 Kasper polyhedron,[45] with a hexagonal symmetry axis (two aligned disclination lines), which is visible in Fig. 1. Note that there is one atom at the center of the Z14 polyhedron, adding up to a total of 15 core atoms. All the Li atoms are in the core. The Na shell is grown by covering the triangular faces and the apex sites of the Z14 polyhedron. This would lead to a geometrical shell closing for a cluster with 51 atoms. The excess of 4 Na atoms is what causes the surface distortions appreciated in Fig. 1. The GM structures for $x=14-16$ are similar, but now the core contains 16 atoms and is based on the Z15 Kasper polyhedron,[45] with three negative disclination lines.

The number of core atoms, N_c, is an important structural descriptor. It changes abruptly from 13 to 15 at $x=8$. Even if there were structures with 14 core atoms in our database, none of them became the most stable one. The increase in N_c is expected because of the size mismatch between Li and Na atoms: the core may house more atoms if those atoms are smaller. There are also energetic factors: while for $x=1$ the Li impurity alleviates the core stress in the Mackay icosahedron, many Li impurities induce a large tensile strain because of too long Li–Li bonds and nonoptimal Li–Na bonds.

It is interesting that the Kasper structures are also the GM in the Li-rich side for $x=36-42$. In this range, the stability of the Mackay icosahedron is reduced because additional Na atoms should occupy surface edge sites. The Z14 and Z15 structures provide additional vertex sites for the Na atoms. Also, the Na surface atoms help releasing the stress of the more compact Kasper structures.

For compositions $x=17-35$, the structures show polyicosahedral (p-Ih) packing. The Li component itself also adopts p-Ih packing, while the Na atoms form an overlayer covering the faces and apex of the Li core. As x increases, a larger proportion of Li atoms is on the cluster surface. In those cases, the Na atoms preferentially cap the triangular faces of the Li core in order to maximize the number of Li-Na bonds (see $x=29$ in Fig. 1 as an example). A complete covering of the Li core (i.e., a perfect core-shell structure) is obtained only for $x=16-18$. For $x=19$, the Li part is a double icosahedron formed by two interpenetrating 13-atom icosahedra. For $x=23$ and $x=26$, there are respectively three and four interpenetrated Li_{13} icosahedra.

The Gupta GM structures for Na_xK_{55-x} do not exactly coincide with those of Li_xNa_{55-x} for most compositions. However, the structural families identified are the same, and the main differences are the critical compositions. On the Na-rich side, the Mackay icosahedron is stable for $x=43-54$, but on the K-rich side, it is only stable for $x=1-6$. The structures based on Kasper polyhedra have a wider stability range on the Na-rich side, namely, for $x=34-42$, but a narrower one ($x=7-8$) on the K-rich side. The rest of compositions show p-Ih packing. In general, the structures tend to be slightly more symmetric for the Na–K alloy, with a smaller dispersion in the bond lengths. A highly symmetric structure containing a Z14 core is shown in Fig. 1 for $x=34$ from two different perspectives. In the second view, a tendency to form sandwichlike structures (in which the K atoms cover two opposite sides of the Na component) can be appreciated. This happens also for other compositions.

B. DFT structures

1. Li–Na alloys

Figure 2 shows a selection of the DFT structures of Li_xNa_{55-x}. On the Na-rich side, the Mackay icosahedron is stable for $x=1-9$, with substitutional Li atoms in the cluster core. A subtle difference with respect to the Gupta potential is that the core shows partial mixing of Li and Na species. For example, $x=7$ favors a sandwichlike core with the Na atoms occupying two opposing faces of the 13-atom icosahedron. On the Li-rich side, the Mackay icosahedron is stable for $x=45-54$, with the substitutional Na atoms occupying vertex sites on the surface. This is a narrower range as compared to Gupta predictions.

Thus, a general effect of the DFT reoptimizations is to shift the critical compositions predicted by the empirical models. However, the most dramatic effect is that all the structures based on the Z14 and Z15 Kasper polyhedra dis-
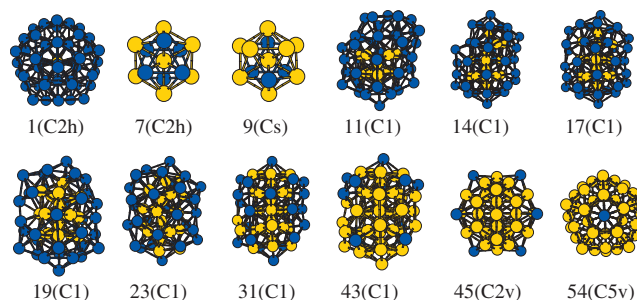

FIG. 2. A representative selection of the putative GM structures of Li_xNa_{55-x} nanoalloys as predicted by DFT calculations. For $x=7$ and $x=9$, we show just the 13-atom core. The color coding is the same as in Fig. 1.

appear from the list of putative GM, which are instead based on p-Ih packing for compositions $x = 10-44$. The p-Ih structures themselves are also different from their Gupta counterparts. The core contains 15 atoms for $x = 10-12$ and 16 atoms for $x = 13-16$, and is a fragment of the 19-atom double icosahedron. $x = 16-17$ are compositions close to a perfectly segregated core-shell structure. For $x = 19$, the Li component forms a double icosahedron, which is nevertheless quite distorted and not uniformly covered by the shell of Na atoms. For larger x values, the Li_{13} icosahedra prefer to be packed along a single direction, forming structures with a marked prolate deformation ($\beta = 0.2$ and $\gamma = \pi/17$ for $x = 31$).

The electron shell effect favors a prolate distortion for 55-electron metal clusters.[55] It is a nice finding that the electronic structure preferences, which are frustrated in the pure clusters due to the presence of a highly stable icosahedral structure, may be realized in the nanoalloys due to a larger structural freedom. The Z14 and Z15 structures are more spherical, with $\beta \approx 0.06$, and are penalized at the DFT level, lying 0.8 eV above the GM for $x = 39$, for example.

2. Na–K alloys

Figure 3 shows some structures for Na_xK_{55-x} nanoalloys. The stability range of the Mackay icosahedron is further reduced compared to the Li–Na alloys. On the K-rich side ($x = 1-5$), the substitutional Na impurities occupy different radial shells of the icosahedron. Therefore, there is no segregation of the Na component to the cluster core in this dilute limit. On the Na-rich side, the Mackay icosahedron is stable for $x = 46-54$. For $x = 54$, the single K impurity substitutes a Na surface vertex, but substitution in a surface edge is just 0.11 meV/atom less stable. For $x = 53$, the two K atoms occupy two opposite surface edge positions. For $x = 46-52$, the K atoms start covering two opposite faces of the Mackay icosahedron, leading to partial segregation within the surface shell.

The DFT GM structures for $x = 6-45$ are all based on p-Ih packing and adopt elongated prolate shapes. The most important difference with respect to Li–Na is that Na–K nanoalloys have more perfect structures, many of which have a nontrivial rotational symmetry. The higher structural order is reminiscent of the bulk situation, where only Na–K alloys form an ordered intermetallic phase. The core has 15 atoms for $x = 6-11$, 16 atoms for $x = 12-14$, and 17 atoms for $x = 15-17$ so that $x = 17$ is a perfect core-shell structure. For $x = 13$, a Na_{13} icosahedral subunit is formed at the core, and the nanoalloy can be seen as a perfect 45-atom polyicosahedron capped with 10 K adatoms. $x = 18$ is the other perfect core-shell structure based on the 19-atom double icosahedron. This would happen at $x = 19$ for 56-atom clusters, with a K shell completely covering the Na_{19} double icosahedron. For larger x, several Na_{13} icosahedra are packed along the same spatial direction, generating highly prolate distortions. For $x = 41$, the K shell tends to cover just one side of the Na subsystem ("ball and cup" arrangement[22]). All the putative GM structures, together with their point group symmetries, are available as supplementary material.[61]
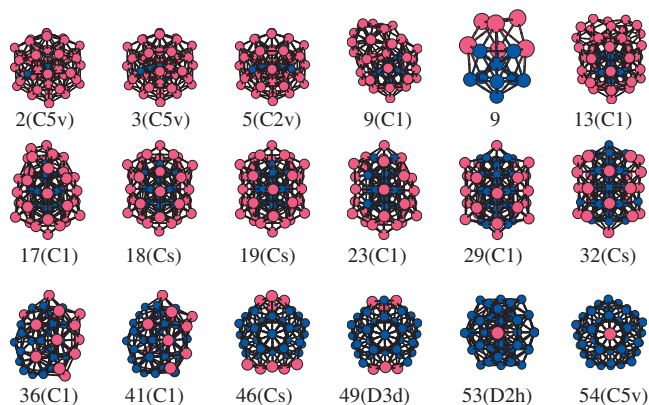

FIG. 3. A representative selection of the putative GM structures of Na_xK_{55-x} nanoalloys as predicted by DFT calculations. For $x = 9$, we show both the cluster and its core. The color coding is the same as in Fig. 1.

C. Nanoalloy stability

Figures 4 and 5 show the DFT cohesive energies, excess energies, and Δ_2 values for Li_xNa_{55-x} and Na_xK_{55-x}, respectively. The cohesive energies are positive for all compositions, indicating that the clusters are stable. The excess energies are typically negative, so mixing is an exothermic process. The maximum deviation of the cohesive energy with respect to the average (or the minimum in the excess energy) occur for $x = 19$, suggesting that this is the most stable composition. For $x = 2-6$, the excess energies are positive for Na–K, so there may be a barrier to the incorporation of a few Na atoms into a potassium cluster host. Also, doping of a pure Na cluster with few K atoms is a weakly exothermic process.

The magical composition at $x = 19$ is driven for both nanoalloys by the high stability of a core-shell polyicosahedral arrangement in which the atomic species of bigger size tends to segregate to the surface. The core-shell arrangement releases much of the strain inherent to p-Ih structures. This is the main factor explaining the location of the magical composition, but it cannot be the only factor, as the perfect core-shell structures occur for $x = 16, 17$ in Li–Na alloys and $x = 17, 18$ in Na–K alloys. Clearly the high stability and compactness of the 19-atom double-icosahedral core are a secondary but important factor.

Li–Na nanoalloys have more negative excess energies than Na–K nanoalloys, the opposite trend as compared to the bulk limit. Li–Na alloys exhibit extensive immiscibility in both solid and liquid phases.[62] On the contrary, Na–K alloys show an intermetallic hexagonal solid phase for KNa_2 and are miscible.[63] The Li–Li bond is much stronger than the Na–Na bond, favoring phase segregation in the bulk limit. Therefore, there should be a critical nanoalloy size above which Na and Li show phase separation, but for the small cluster size considered here, mixing is still very favorable. In the bulk limit, the contribution of the Li–Na interface is negligibly small, while this is not the case for a finite system. The core-shell structures allow for an optimal p-Ih packing of the interior Li atoms (by releasing the core stress) while taking advantage of the heteroatomic bond contribution to the total cluster energy.
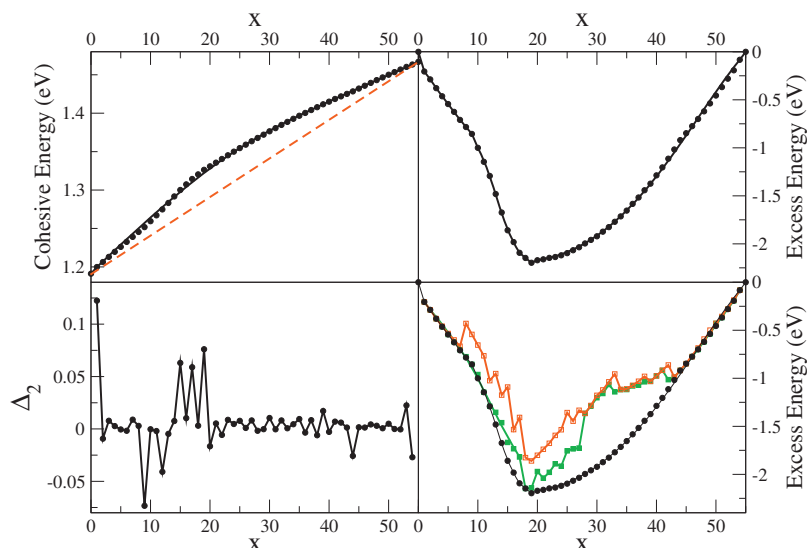
FIG. 4. Results on the Li_xNa_{55-x} energetics. Upper left graph: DFT cohesive energy as a function of composition x. The dashed line is a linear interpolation between the cohesive energies of the pure clusters. Upper right graph: DFT excess energy. Lower left graph: second-order difference Δ_2. Lower right panel: a comparison of several excess energy curves.

The Δ_2 values show compositions for which the nanoalloy is more stable than the average of its two neighboring compositions. Apart from the magical composition $x=19$, these are $x=1,15,17$ for Li–Na and $x=1,13$ for Na–K nanoalloys. $x=1$ is a very stable composition, and for Li–Na nanoalloys, $x=1$ indeed has the largest Δ_2 value. As shown by Mottet et al.,[17] the substitution of a small size impurity into the central position of an icosahedron helps releasing the cluster stress and stabilizes the doped cluster. The high relative stability of $Na_{13}K_{42}$ is related to the formation of a compact 45-atom polyicosahedral fragment, which cannot be formed for other compositions.

We compare several excess energy curves on the lower right graphs in Figs. 4 and 5. The red curve is the one obtained after DFT reoptimization of the Gupta global minima. The green curve is obtained after reoptimizing the 50 lower energy Gupta isomers for each composition and then choosing the one with the lowest DFT energy. The black curve is the optimal DFT excess energy. While the converged curve is smooth, the behavior of the other two curves is quite erratic, which is an indication of poor convergence. We see that the Gupta potential is relatively more reliable in both dilute com-

position limits (mostly for Li–Na alloys) and also for perfect core-shell structures. The offered comparison serves as a visual demonstration for the accuracy of our methodology: (a) consider the EP just as a generator of structural diversity; (b) choose different structural motifs for DFT reoptimization based on some structural indicators; and (c) apply the composition comparison approach self-consistently at the DFT level.

D. Other structural and electronic properties

Figure 6 shows the VIP and VEA of Li–Na and Na–K nanoalloys as a function of composition. For Li–Na, the VIP decreases on average upon doping the icosahedral host so that the HOMO gets more and more destabilized. The transition toward the prolate p-Ih structures comes with a significant stabilization of the HOMO. In fact, the VIP of the p-Ih structures is higher than the weighted average of the pure clusters, which means that the excess VIP is a positive quantity. The stabilization of Li–Na nanoalloys has therefore an electronic contribution for most compositions. For Na–K
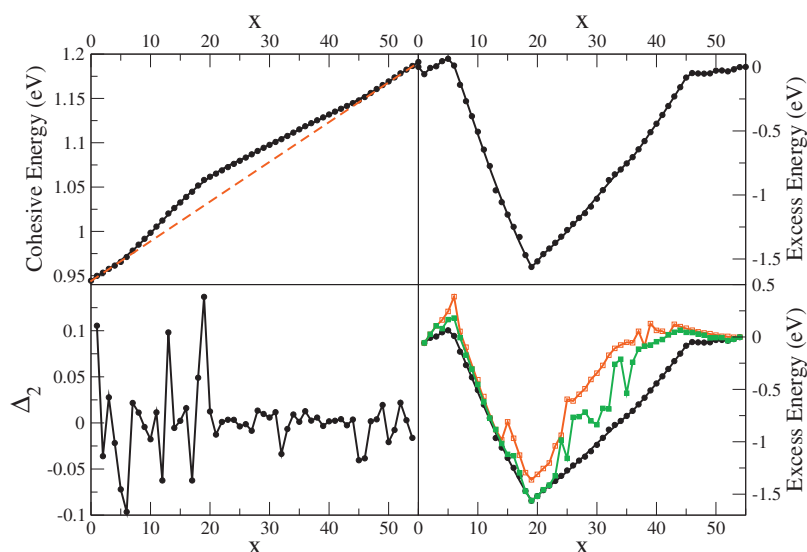

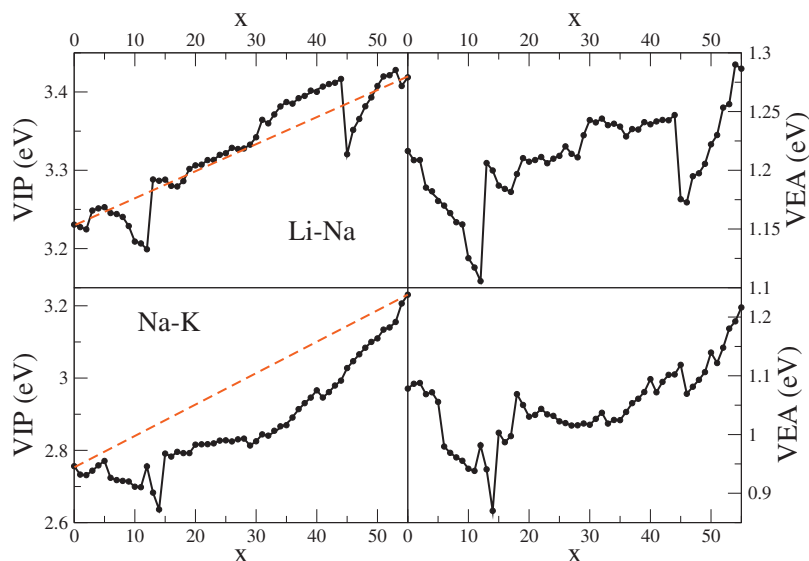FIG. 5. Results on the Na_xK_{55-x} energetics. The meaning of the different graphs is the same as in Fig. 4.

FIG. 6. Vertical ionization potential (graphs on the left side) and vertical electron affinity (graphs on the right side) of Li_xNa_{55-x} and Na_xK_{55-x}. The dashed line is a linear interpolation between the two pure clusters.

nanoalloys, all compositions have negative excess VIP values so that the HOMO level is always destabilized upon mixing.

Figure 7 shows the electronic DOS of Na–K nanoalloys for selected compositions. Each level is broadened in order to simulate photoelectron spectra, which provide a structural fingerprint for pure metal clusters,[56,57] so it is interesting to check if they are also sufficiently sensitive as a structural probe for nanoalloys of fixed size and varying composition. The upper left panel shows typical DOS for K-rich alloys. Introducing a sodium impurity ($x=1$) hardly changes the shape of the DOS but induces shifts in the positions of the several peaks. For $x=5$, the perturbation is already sufficiently strong as to change the shape of the DOS to a detectable degree, even if the structure remains icosahedral. On the Na-rich side (lower right graph), the incorporation of up to nine K atoms does not modify the shape of the DOS but induces large and measurable shifts in the peak positions. The DOSs of all remaining compositions are very different from the icosahedral ones. $x=19$, for example, has a well structured DOS due to its high structural symmetry. Other compositions such as $x=9$ have a less structured and very different spectrum. Even similar structures from the highly prolate p-Ih family ($x=32$ and 41 in Fig. 7) have clearly distinguishable DOSs. Therefore, photoelectron spectroscopy might confirm (or contradict) the reliability of the putative GM presented in this paper. We hope that our results will motivate future experimental research on alkali nanoalloys.

It is interesting to note that the electronic ground state of the p-Ih structures is a spin doublet, while for the icosahedral structures (i.e., the pure and the substitutionally doped clusters), it is a spin quartet. So the transition between those two structural families is also a spin (magnetic) transition. For the icosahedral structures, the quartet is more stable than the doublet by about 0.05–0.08 eV depending on the system and composition. For the p-Ih structures, the doublet is more stable than the quartet by about the same energy. The spin multiplicity is therefore important in the determination of the critical compositions.

The excess radii of the nanoalloys are shown in Fig. 8. Except for a few compositions, both Li–Na and Na–K nanoalloys have negative excess radii, i.e., they are more
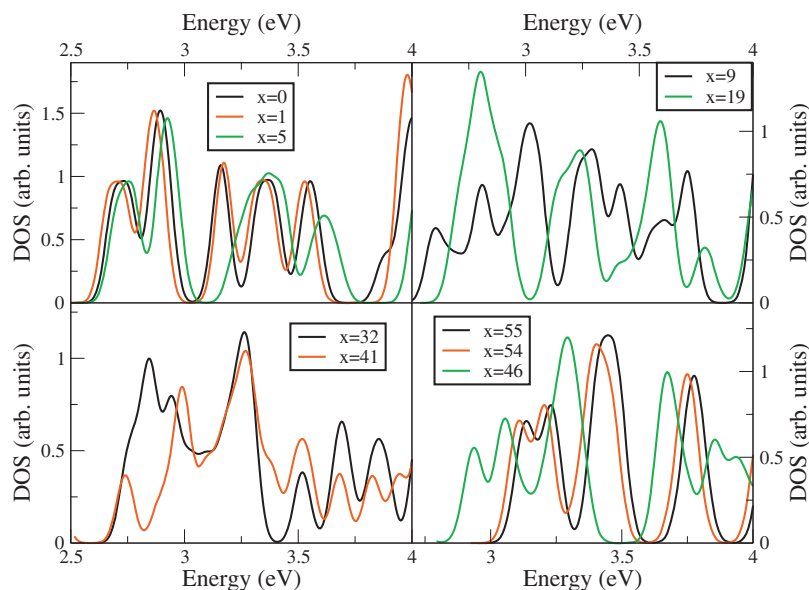

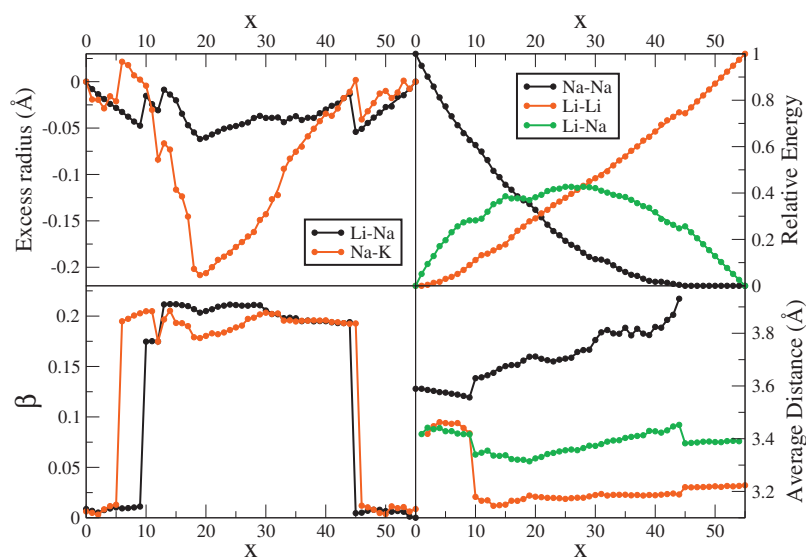FIG. 7. Electronic DOS of Na_xK_{55-x} for selected compositions.

FIG. 8. Upper left graph: Excess cluster radius of Li_xNa_{55-x} and Na_xK_{55-x}. Lower left graph: Hill–Wheeler β parameter. Upper right graph: an estimation of the relative contribution of Na–Na, Li–Li, and Li–Na bonds to the total cohesive energy of Li_xNa_{55-x}. Lower right graph: average lengths of Na–Na, Li–Li, and Li–Na bonds.

compact than the pure metal clusters. At intermediate compositions, this is induced by the polyicosahedral packing, which is known to be more compact than the icosahedral one. The relative compactness is much higher in Na–K than in Na–Li nanoalloys. This suggests that the size and bond strength mismatches comply so that Na and K subsystems fit more perfectly than Li and Na. Comparing the excess radii and the VIP shown in Fig. 6, one can conclude that structural effects dominate the stabilization of Na–K nanoalloys, while both structural and electronic effects are important for Li–Na nanoalloys.

The lower left graph in Fig. 8 shows the composition dependence of the shape parameter β. It is an ideal order parameter to describe the spherical (icosahedral) to prolate (p-Ih) transitions. It is clearly seen that the range of stability of the p-Ih structures is wider for the Na–K nanoalloys. Such a change in the global shape should be easily identified in measurements of cluster mobilities.[64]

Although a partitioning of the DFT total energy into different contributions cannot be done in a unique way, we have estimated the relative contributions of homoatomic and heteroatomic bonds to the cluster energy as follows. First, we have determined the total number of A-A, B-B, and A-B bonds. We assume that two like atoms are bonded whenever their distance is less than a cutoff, fixed to 10% longer than the longest bond in the corresponding Mackay icosahedron. The cutoff distance for A-B bonds is the arithmetic mean of the A-A and B-B cutoffs. The energy of an A-A (or B-B) bond is obtained by dividing the total energy of A_{55} (or B_{55}) by the total number of bonds in the Mackay icosahedron. The energy of an A-B bond is the arithmetic mean of the A-A and B-B energies. We show in the upper right panel of Fig. 8 the normalized relative contribution of each type of bond to the total cluster energy as a function of composition. Although this plot is not meant to be quantitative, it clearly shows that at the magical composition $x=19$, all bonds contribute appreciably, and heteroatomic bonds make the dominant contribution to the total energy. An optimal packing of the A-core and B-shell is therefore a crucial aspect of the stability of this composition. The lower right panel shows the

average distances for each type of bond in Li–Na nanoalloys. A minimum is observed at $x=19$ for the Li–Na distance, which is shorter than in the dilute limits. The core-shell arrangement achieves thus an optimal packing of the Li core and the Na-shell (the minimum is more marked in the Na–K results, which are not shown explicitly). The Li–Li average distance is slightly shorter than for the Li_{55} icosahedron mostly because all Li atoms are in the cluster core. Na–Na bonds are already very strained at $x=19$ as compared to the typical values of surface bonds in a Na icosahedron. A similar plot for Na–K (not shown explicitly) shows that the K–K surface bonds are not appreciably distorted for $x=19$. The size mismatch in Na–K is therefore more optimal for the stability of the core-shell structure than in Li–Na mixtures. This rationalizes the different behaviors of the two nanoalloys, with substantial distortions for Li–Na due to the frustration of Na–Na bonds and more perfect structural order in Na–K.

The analysis of atomic charges reveals a very small degree of charge transfer. For most compositions, charge flows in the expected direction according to electropositivity arguments, i.e., from the Na-shell to the Li core in Li–Na alloys and from the K shell to the Na core in Na–K alloys. The charge transfer is systematically smaller in Na–K alloys as compared to Li–Na alloys. For example, the average lithium charge in $Li_{19}Na_{36}$ is about -0.035 for both VDD and Bader measures, while the average sodium charge in $Na_{19}K_{36}$ is -0.021 (VDD) or -0.015 (Bader). The different definitions of atomic regions in VDD and Bader methods do not result in significantly different charges, so we believe that the predicted charge transfer picture is reliable. The charge transfer discussed here is not related to electron localization, and should be interpreted as an accumulation or depletion of electron density within the atomic volumes.

Interesting differences between both methods emerge for substitutional impurities. For example, the lithium charge in Li_1Na_{54} is -0.065 (VDD) or $+0.055$ (Bader). As shown in Fig. 8, the Li–Na distance is too expanded in Li_1Na_{54}. The sodium host cluster contracts upon doping but only to a limited extent due to steric reasons. The VDD method therefore

assigns too large a Voronoi volume to the central impurity. In our view, the Bader result is more reliable here, and it predicts that electron charge flows from the central Li atom to the 12 nearest-neighbor Na atoms. This is a sensible result: because of the host compression, the Na–Na bonds near the Li impurity are shorter than in Na_{55}, so more electron charge is needed there in order to screen the increased ionic repulsion. Qualitative differences between the two methods are only detected for substitutional impurities, for which the rigidity of the host structure forces nonoptimal heteroatomic bond lengths.

IV. SUMMARY AND DISCUSSION

Putative GM structures of Li_xNa_{55-x} and Na_xK_{55-x} nanoalloys have been presented. The structures have been obtained through an unbiased search procedure, which combines parametrized potentials and first-principles DFT methods. The structure of the 55-atom pure metal clusters (a perfect Mackay icosahedron) is preserved in the nanoalloys at the dilute concentration limits, i.e., the atoms of the minority component are incorporated into the icosahedron as substitutional impurities. For intermediate compositions, a polyicosahedral packing is more favorable. In most cases, the structures show core-shell segregation, with the atomic species of bigger size and lower surface tension preferentially occupying the surface shell. The p-Ih structures are strongly prolate, in agreement with the predictions of the jellium model for 55-atom metal clusters. The electronic preference for a prolate ionic density is satisfied in nanoalloys, while it is frustrated in pure alkali clusters due to the presence of a geometrical shell closing for icosahedral growth. There are subtle but interesting structural differences between Li–Na and Na–K nanoalloys. The stability range of the p-Ih structures is wider for Na–K. At intermediate compositions, the GM structures of Na_xK_{55-x} have a high structural order with little bond length dispersion, while those of Li_xNa_{55-x} undergo strong distortions away from the perfect p-Ih shapes.

There are significant differences between DFT and EP structure predictions. First, the empirical potential GM includes structures based on the Z14 and Z15 Kasper polyhedra for a range of compositions. These structures are quite spherical with a slight triaxial deformation and are strongly penalized at the DFT level. They might still be relevant for other cluster sizes such as $N=58$, which favor more spherical shapes. Second, the p-Ih EP structures are much more spherical than their DFT counterparts quite probably because of the neglect of quantum electronic shell effects in the EP models. Third, although the general preference for core-shell structures is the same, the detailed segregation properties differ in both models; according to DFT, there is some mixing of Li and Na species within the core on the Na-rich side of Li_xNa_{55-x} nanoalloys, while the EP models predict segregation of those two species within the core. Also, there is no core-shell segregation on the K-rich side of Na_xK_{55-x}, although the EP models predict it. Finally, the composition ranges over which icosahedral and p-Ih structures are stable also differ.

The excess energies are negative with the exception of some K-rich Na_xK_{55-x} nanoalloys, so mixing is an exothermic process. The minimum excess energy is located at the *magical composition $x=19$*. At this composition, the species with smaller size and stronger bonds forms a compact double icosahedron structure at the cluster core. The nanoalloy formation process is about 0.5 eV more exothermic for Li–Na than for Na–K. This is opposite to the bulk situation where Li and Na show extended immiscibility, while Na and K are miscible. The analysis of the second-order energy difference shows that $x=1$ is another very stable composition. This is explained by the stress release accompanying the introduction of a small substitutional impurity at the central position of a Mackay icosahedron.

An analysis of the vertical ionization potential shows that the HOMO level is stabilized in Li–Na but destabilized in Na–K alloys, as compared to the corresponding pure metal limits. This suggests a favorable electronic contribution to the excess energies only for Li–Na alloys, which might partially explain their higher stability. The excess radii show that both alloys become more compactly packed at the magical composition, as compared to the pure metals. The Na–K alloys, however, are more compact than Li–Na alloys, with a more perfect fit between core and surface shells. The analysis of the VDD and Bader atomic charges demonstrates that charge transfer is very small in magnitude for both alkali mixtures, and its direction agrees with the electropositivities of alkali atoms.

The transition between Ih and p-Ih structures is accompanied by an abrupt change in the magnetic moment and also in the cluster shape. The shape change should be detectable in mobility experiments where the collision cross sections of clusters are measured. Similarly, our DOS results suggest that photoelectron spectroscopy, a usual technique to deduce the structures of pure metal clusters, would also be useful in deducing gross features of the structures of nanoalloys.

The present work identified trends in the structural and chemical ordering patterns for alkali nanoalloys of fixed size and small size mismatch. Our prospects for the future include the analysis of the effect of a larger size mismatch, for example, in Li–Cs nanoalloys. In the longer term, we plan to study structural trends in nanoalloys of varying sizes.

[1] A. M. Molenbroek and J. K. Norskov, J. Phys. Chem. B **105**, 5450 (2001).
[2] H. Yasuda and H. Mori, Phys. Rev. Lett. **69**, 3747 (1992).
[3] H. Portales, L. Saviot, E. Duval, M. Gaudry, E. Cottancin, M. Pellarin, J. Lermé, and M. Broyer, Phys. Rev. B **65**, 165422 (2002).
[4] J. P. Wilcoxon and P. P. Provencio, J. Am. Chem. Soc. **126**, 6402 (2004).
[5] C. Burda, X.-B. Chen, R. Narayanan, and M. A. El-Sayed, Chem. Rev. (Washington, D.C.) **105**, 1025 (2005).
[6] M. Tchaplyguine, S. Legendre, A. Rosso, I. Bradeanu, G. Öhrwall, S. E. Canton, T. Andersson, N. Mårtensson, S. Svensson, and O. Björneholm, Phys. Rev. B **80**, 033405 (2009).
[7] M. J. López, P. A. Marcos, and J. A. Alonso, J. Chem. Phys. **104**, 1056

(1996).

[8] J. Jellinek and E. B. Krissinel, Chem. Phys. Lett. **258**, 283 (1996); E. B. Krissinel and J. Jellinek, *ibid.* **272**, 301 (1997).

[9] S. Huang and P. B. Balbuena, J. Phys. Chem. B **106**, 7225 (2002).

[10] K. Joshi and D. G. Kanhere, J. Chem. Phys. **119**, 12301 (2003).

[11] S. Chacko, D. G. Kanhere, and V. V. Paranjape, Phys. Rev. A **70**, 023204 (2004).

[12] A. Aguado, L. E. González, and J. M. López, J. Phys. Chem. B **108**, 11722 (2004); A. Aguado, S. Núñez, and J. M. López, Comput. Mater. Sci. **35**, 174 (2006).

[13] A. Aguado and J. M. López, Phys. Rev. B **71**, 075415 (2005).

[14] A. Aguado and J. M. López, J. Chem. Theory Comput. **1**, 299 (2005).

[15] A. Aguado and J. M. López, Phys. Rev. B **72**, 205420 (2005).

[16] J. P. K. Doye and L. Meyer, Phys. Rev. Lett. **95**, 063401 (2005).

[17] C. Mottet, G. Rossi, F. Baletto, and R. Ferrando, Phys. Rev. Lett. **95**, 035501 (2005).

[18] A. A. Dzhurakhalov and M. Hou, Phys. Rev. B **76**, 045429 (2007).

[19] F. Calvo, E. Cottancin, and M. Broyer, Phys. Rev. B **77**, 121406(R) (2008).

[20] Z. Kuntová, G. Rossi, and R. Ferrando, Phys. Rev. B **77**, 205431 (2008).

[21] L. O. Paz-Borbón, R. L. Johnston, G. Barcaro, and A. Fortunelli, J. Chem. Phys. **128**, 134517 (2008).

[22] L. O. Paz-Borbón, A. Gupta, and R. L. Johnston, J. Mater. Chem. **18**, 4154 (2008).

[23] R. Ferrando, A. Fortunelli, and R. L. Johnston, Phys. Chem. Chem. Phys. **10**, 640 (2008).

[24] E. Hristova, V. G. Grigoryan, and M. Springborg, J. Chem. Phys. **128**, 244513 (2008); Eur. Phys. J. D **52**, 35 (2009).

[25] L. Delfour, J. Creuze, and B. Legrand, Phys. Rev. Lett. **103**, 205701 (2009).

[26] F. Pittaway, L. O. Paz-Borbón, R. L. Johnston, H. Arslan, R. Ferrando, C. Mottet, G. Barcaro, and A. Fortunelli, J. Phys. Chem. C **113**, 9141 (2009).

[27] D. J. Borbón-González, R. Pacheco-Contreras, A. Posada-Amarillas, J. C. Schön, R. L. Johnston, and J. M. Montejano-Carrizales, J. Phys. Chem. C **113**, 15904 (2009).

[28] J. A. Reyes-Nava, J. L. Rodríguez-López, and U. Pal, Phys. Rev. B **80**, 161412(R) (2009).

[29] D. T. Tran and R. L. Johnston, Phys. Chem. Chem. Phys. **11**, 10340 (2009).

[30] I. Parsina and F. Baletto, J. Phys. Chem. C **114**, 1504 (2010).

[31] Y. Gao, N. Shao, Y. Pei, and X. C. Zeng, Nano Lett. **10**, 1055 (2010).

[32] G. E. Ramírez-Caballero and P. B. Balbuena, J. Phys. Chem. Lett. **1**, 724 (2010).

[33] R. Ferrando, J. Jellinek, and R. L. Johnston, Chem. Rev. (Washington, D.C.) **108**, 845 (2008).

[34] D. J. Wales, J. P. K. Doye, A. Dullweber, M. P. Hodges, F. Y. Naumkin, F. Calvo, J. Hernández-Rojas, and T. F. Middleton, The Cambridge Cluster Database (CCD), http://www-wales.ch.cam.ac.uk/CCD.html.

[35] W. D. Knight, K. Clemenger, W. A. de Heer, W. A. Saunders, M. Y. Chou, and M. L. Cohen, Phys. Rev. Lett. **52**, 2141 (1984).

[36] M. Brack, Rev. Mod. Phys. **65**, 677 (1993).

[37] R. P. Gupta, Phys. Rev. B **23**, 6265 (1981).

[38] V. Rosato, M. Guillopé, and B. Legrand, Philos. Mag. A **59**, 321 (1989).

[39] F. Cleri and V. Rosato, Phys. Rev. B **48**, 22 (1993).

[40] M. J. López and J. Jellinek, J. Chem. Phys. **110**, 8899 (1999).

[41] Y. Li, E. Blaisten-Barojas, and D. A. Papaconstantopoulos, Phys. Rev. B **57**, 15519 (1998).

[42] J. Delhommelle and P. Millié, Mol. Phys. **99**, 619 (2001).

[43] J. R. Christman and H. B. Huntington, Phys. Rev. **139**, A83 (1965).

[44] D. J. Wales and J. P. K. Doye, J. Phys. Chem. A **101**, 5111 (1997).

[45] D. J. Wales, *Energy Landscapes* (Cambridge University Press, Cambridge, 2003).

[46] W. Kohn and L. J. Sham, Phys. Rev. A **140**, A1133 (1965).

[47] P. Hohenberg and W. Kohn, Phys. Rev. **136**, B864 (1964).

[48] J. M. Soler, E. Artacho, J. D. Gale, A. García, J. Junquera, P. Ordejón, and D. Sánchez-Portal, J. Phys.: Condens. Matter **14**, 2745 (2002).

[49] J. P. Perdew and A. Zunger, Phys. Rev. B **23**, 5048 (1981).

[50] D. M. Ceperley and B. J. Alder, Phys. Rev. Lett. **45**, 566 (1980).

[51] R. Hamann, M. Schlüter, and C. Chiang, Phys. Rev. Lett. **43**, 1494 (1979).

[52] L. Kleinman and D. M. Bylander, Phys. Rev. Lett. **48**, 1425 (1982).

[53] J. P. Perdew, K. Burke, and M. Ernzerhof, Phys. Rev. Lett. **77**, 3865 (1996).

[54] D. L. Hill and J. A. Wheeler, Phys. Rev. **89**, 1102 (1953).

[55] S. Kümmel, M. Brack, and P.-G. Reinhard, Phys. Rev. B **62**, 7602 (2000).

[56] L. Ma, B. von Issendorff, and A. Aguado, J. Chem. Phys. **132**, 104303 (2010).

[57] K. Majer, M. Lei, C. Hock, B. von Issendorff, and A. Aguado, J. Chem. Phys. **131**, 204313 (2009).

[58] C. F. Guerra, J.-W. Handgraaf, E. J. Baerends, and F. M. Bickelhaupt, J. Comput. Chem. **25**, 189 (2003).

[59] R. F. W. Bader, *Atoms in Molecules. A Quantum Theory* (Clarendon, Oxford, 1990).

[60] M. A. Spackman and E. N. Maslen, J. Phys. Chem. **90**, 2020 (1986); E. N. Maslen and M. A. Spackman, Aust. J. Phys. **38**, 273 (1985).

[61] See supplementary material at http://dx.doi.org/10.1063/1.3479396 for the files containing the atomic coordinates and point group symmetries of the putative GM structures located in this work at both EP and DFT levels of theory.

[62] C. W. Bale, J. Phase Equilib. **10**, 265 (1989).

[63] J. B. Ott, J. R. Goates, D. R. Anderson, and H. T. Hall, Trans. Faraday Soc. **65**, 2870 (1969).

[64] M. F. Jarrold and V. A. Constant, Phys. Rev. Lett. **67**, 2994 (1991).